

Stellar evolution with rotation

XIII. Predicted GRB rates at various Z^*

R. Hirschi¹, G. Meynet², and A. Maeder²

¹ Dept. of physics and Astronomy, University of Basel, Klingelbergstr. 82, 4056 Basel, Switzerland
e-mail: raphael.hirschi@unibas.ch

² Geneva Observatory, 1290 Sauverny, Switzerland

Received 28 April 2005 / Accepted 11 July 2005

ABSTRACT

We present the evolution of rotation in models of massive single stars covering a wide range of masses and metallicities. These models reproduce observations during the early stages of the evolution very well, in particular Wolf-Rayet (WR) populations and ratio between type II and type Ib,c supernovae at different metallicities.

Our models predict the production of fast-rotating black holes. Models with large initial masses or high metallicity end their lives with less angular momentum in their central remnant with respect to the break-up limit for the remnant. Many WR star models satisfy the three main criteria (black hole formation, loss of hydrogen-rich envelope, and enough angular momentum to form an accretion disk around the black hole) for gamma-ray bursts (GRB) production via Woosley's collapsar model. If we consider all types of WR stars as GRB progenitors, there would be too many GRBs compared to observations but if we consider only WO stars (type Ic supernovae as is the case for SN2003dh/GRB030329) as GRB progenitors, the GRB production rates are in much better agreement with observations. WO stars are produced only at low metallicities in the present series of models. This prediction can be tested by future observations.

Key words. stars: evolution – stars: rotation – stars: Wolf-Rayet – stars: supernova: general – gamma rays: theory – gamma rays: bursts

1. Introduction

In the previous papers of the series on stellar evolution with rotation, the effects of rotation on the stellar evolution was studied with an emphasis on the early stages of the pre-supernova evolution (main sequence, MS, and He-burning). The models reproduce many observational features at various metallicities very well, like surface enrichment (Meynet & Maeder 2002b) and ratios between red and blue supergiants (Maeder & Meynet 2001, hereinafter Paper VII). In Meynet & Maeder (2005, Paper XI) and Meynet & Maeder (2003, Paper X), the Wolf-Rayet (WR hereinafter) star population at different metallicities are studied. In view of the lower mass loss rates obtained when clumping effects in the winds are accounted for, models without rotation do not reproduce the WR populations in galaxies. Models of rotating massive stars give a much better fit to the populations of WR stars at different metallicities than do non-rotating models. They can reproduce the observed number ratio of WR to O-type stars, the observed ratio of WN to WC stars (for metallicities lower than solar), the observed fraction of WR stars in the transition phase WN/WC,

and finally the observed ratio of type Ib and Ic to type II supernovae. A good fit of the observed properties of WR stars is of particular interest in this study, since WR stars are thought to be progenitors of GRBs.

In Hirschi et al. (2004, hereinafter Paper XII), we described the recent modifications made to the Geneva code and the evolution of the models until silicon burning. In this paper, we look at the evolution of rotation in massive stars with an emphasis on the final stages of the evolution towards neutron stars (NS), black holes (BH), and especially long soft γ -ray bursts (GRB).

1.1. Neutron stars

There are many observations of neutron stars and pulsars available. A catalogue of observed pulsars and their properties is available at the web page of the group ATNF (2005). The fastest young pulsars have periods larger than 10 ms: 16 ms for J0537-6910 (Marshall et al. 1998), 33 ms for the Crab pulsar (B0531+21, Staelin & Reifenstein 1968), and 50 ms for J0540-6919 (Seward et al. 1984). There are about 20 pulsars with a period smaller than 100 ms in the catalogue and an age less

* Tables 4–7 are only available in electronic form at <http://www.edpsciences.org>

than 100 000 years. The pulsars may have slowed down slightly since their birth but the initial period of pulsars is at least 10 ms. NS are supposed to form during the collapse of stars with an initial mass between about 10 and $25 M_{\odot}$. If we compare 10 ms with the values obtained in Tables 4–7 (Cols. 11 and 12), we see that in general our models have much more angular momentum than the observed pulsars. The difference can reach a factor of about 100 around $15 M_{\odot}$ and a factor of about 10 around $60 M_{\odot}$. In order to reconcile the model predictions with the observations, additional angular momentum has to be lost before the formation of the pulsar. This can occur during the pre-supernova stages due to the effects of the magnetic fields not taken into account in this work or else during the collapse and the explosion. The existence of a primordial magnetic field in some stars (Braithwaite & Spruit 2004) may also slow down their core. Models including the effects of magnetic fields have only recently been developed (Heger et al. 2004; Maeder & Meynet 2004) due to the complexity of the interplay between rotation and magnetic fields. Heger et al. (2005) show that the braking by magnetic fields, which are produced by differential rotation during the evolution (see Spruit 2002) significantly reduce the discrepancy between the predicted and observed pulsar periods. However, these models, as well as binary models presented in Petrovic et al. (2005), contain too little angular momentum at the pre-supernova stage to produce GRBs.

In this paper, we study the case without magnetic field, which is more favourable to GRB production. The case with magnetic braking will be treated in a later study. In addition, the present study offers a basis of comparison for future models that include magnetic fields. It is important here to note that internal magnetic braking is most efficient during the Red SuperGiant (RSG) phase, during which the star has a fast rotating core and a slow rotating envelope. This means that magnetic braking is much less effective for stars which skip the RSG stage, as mentioned in Heger et al. (2005). These stars are the most massive WR stars, with masses larger than about $60 M_{\odot}$. Furthermore, more massive stars have shorter lifetimes and thus less time to be slowed down. It is also possible that mechanisms that slow the nascent neutron star down may not be as efficient when a black hole is formed. These differences between stars with masses around $15 M_{\odot}$ (forming a neutron star and going through the RSG stage) and $60 M_{\odot}$ (not going through the RSG phase and forming black holes) could possibly explain, with the same physics, the pulsar periods and the GRBs. Further studies will verify this possibility.

Braking between the collapse and the pulsar formation can also occur via different mechanisms: r-Mode instability, neutrino-powered magnetic stellar winds, fall-back, and the propeller mechanism. However, these mechanisms may not be efficient enough to slow the core down efficiently (see Heger et al. 2005, for a discussion). The latest models studying gravitational waves seem to indicate that braking is possible during and after the collapse (Ott et al. 2005). If the cores are not slowed down during the pre-supernova stages, rotation may play an important role in supernova explosions. Rotation may in this case provide a large amount of energy for the explosion ($\sim 10^{52}$ erg), but this is generally not observed (Janka et al. 2005).

1.2. Black holes and γ -ray bursts

Theoretical models still struggle to reproduce supernova explosions (for a discussion and references, see Fryer & Heger 2005). It is therefore not possible for us to predict the fate of the remnant of our models with certainty or precision. Nevertheless, following the estimates presented in Fryer (1999) and Heger et al. (2003), we will consider in this study that the lower mass limit for black hole formation is around $25 M_{\odot}$. The upper mass limit depends strongly on the mass loss and is around $100 M_{\odot}$ at solar metallicity. The maximum neutron star mass is also still uncertain (see Srinivasan 2002; Morrison et al. 2004, for recent studies). Depending on the nuclear equation of state used and the rotation rate, the upper mass limit for neutron stars can vary between 1.6 and $3 M_{\odot}$ although 2 to $2.5 M_{\odot}$ is a more common range. BHs cannot be observed directly. Thus they are usually detected in X-ray binaries. In certain cases, observations allow the masses of the binary companions to be determined. If the accreting object has a derived mass larger than $2\text{--}3 M_{\odot}$, it is considered a BH candidate. The best known candidates are LMC X–3 and Cyg X–1 (see Kaper & van der Meer 2005, and references therein).

GRBs can be divided into two main types: a) short and hard and b) long and soft. See Piran (2005) for a recent review of GRBs. The long soft GRBs have recently been connected to supernova (SN) explosions of the type Ib,c (see for example Matheson 2003). Since then, several studies have been devoted to finding which stars can lead to GRBs. Heger et al. (2004), Heger et al. (2005), and Hirschi et al. (2004) looked at massive single star at solar metallicity as progenitors. Note that the two models differ in the treatment of meridional circulation, which is an advective process (Meynet & Maeder 2002a). Our models account for the advection of angular momentum during the MS phase, while models of Heger and collaborators treat meridional circulation as a diffusive process. Maeder & Meynet (2005) show that the treatment of meridional circulation as an advective process is crucial for modelling the interplay between circulation and magnetic braking. Another difference in this article is the fact that we study the effects of metallicity in detail in the context of GRBs for models of differentially rotating stars. This is important since metallicities lower than solar are expected to be more favourable to the production of GRBs (due to weaker mass loss, see MacFadyen & Woosley 1999; Woosley & Heger 2003). Podsiadlowski et al. (2004) and Izzard et al. (2004) considered both single and binary massive stars. Note that Izzard et al. (2004) assume that the loss of angular momentum is proportional to the amount of mass lost and do not consider internal transport of angular momentum. Their approximate treatment of the evolution of angular momentum leads them to the conclusion that only binary stars can retain enough angular momentum in their core to form GRBs. Even without magnetic braking, their models predict no GRBs from single massive stars which is in contradiction with our models and those of Heger et al. (2000). Petrovic et al. (2005) look at single and binary systems with and without magnetic fields at solar metallicity. They find that in the models followed, both single and binary models without magnetic field can produce GRBs and both single and binary models with

magnetic field considered in the study cannot produce GRBs. They conclude that, if the present modelling of magnetic fields is accurate, GRBs have to be produced in some exotic channels of binary systems. Fryer & Heger (2005) looked at massive binary star mergers, which are believed to be one of the best binary candidates for GRBs. They follow the evolution prior to and after the merger with the KEPLER code (Heger et al. 2000) and the merger process with 3D simulations, which is very interesting and which has a lot of potential for further applications. They find that, in some cases, merged helium stars can retain more angular momentum than single massive stars. However, they obtain these faster rotators only for models in which they remove angular momentum artificially without removing mass from the merged star. If more realistic mass loss prescriptions are used after the merger, the final angular momentum contained in the central remnant is similar in merged stars and in single massive stars. This is due to the strong mass loss that WR stars experience, especially the fast rotating ones. Merged stars lose a large amount of mass and some merged systems probably form NSs instead of BHs. It is therefore not proven that binary stars retain more angular momentum than single stars and the exact frequency of potential binary star progenitors has not been compared quantitatively with the GRB rates.

Here we discuss the possibility of single massive stars being progenitors when studying models covering a large range of initial masses and metallicities. These models reproduce the WR star population very well, and many of them retain enough angular momentum to produce GRBs as shown below. We describe the calculations in Sect. 2, the evolution of rotation in Sect. 3, and present our predicted GRB rates in Sect. 4.

2. Description of the calculations

In order to study the evolution of core rotation and its dependence on initial mass and metallicity, we used the models presented in Meynet & Maeder (2003, Paper X) and Hirschi et al. (2004, Paper XII) for solar metallicity and Meynet & Maeder (2005, Paper XI) for non-solar metallicities, which span a wide range in initial masses (9 to $120 M_{\odot}$ at solar metallicity) and metallicities ($Z = 0.004$ to $Z = 0.040$).

All these models (except for one $60 M_{\odot}$ model at $Z = 0.004$) have an initial rotational velocity of 300 km s^{-1} , which gives an average value for the MS of about 220 km s^{-1} , the average observed rotational velocities on the MS (see for example Fukuda 1982). They were all calculated with the same input physics: Schwarzschild criterion for convection, overshooting of $0.1 H_p$ for the hydrogen (H) and helium (He) burning cores, same mass loss prescriptions, and treatment of rotation including meridional circulation and shear diffusion (see Papers X–XII for more details).

Non-solar metallicity models were evolved until the end of core He-burning. Solar metallicity models were evolved until the end of core He-burning for the 9, 85 and $120 M_{\odot}$ models, end of oxygen (O) burning for the $12 M_{\odot}$ model, and end of silicon (Si) burning for the 15, 20, 25, 40, and $60 M_{\odot}$ models. As we shall see later, the largest changes in the angular

momentum of the core occur during H and He-burnings, which is why we did not evolve non-solar metallicity models further than the end of He-burning.

Several quantities are useful for studying the evolution of rotation:

- The angular velocity at mass coordinate m or radius r (here r is the average radius of a shell, see Meynet & Maeder 1997, for details), Ω [s^{-1}], and its ratio to the Keplerian velocity, Ω/Ω_K , where $\Omega_K = \sqrt{Gm/r^3}$. When Ω/Ω_K becomes larger than about 0.9, the star gets elongated along its equator and at break-up, the star equatorial radius is 1.5 times larger than the polar radius (value obtained using the Roche model). Therefore the star may reach break-up before Ω/Ω_K approaches one, in particular for models with a large Eddington factor, which reach break-up for Ω much lower than Ω_K (Maeder & Meynet 2000).
- The angular momentum of a core of mass M , $\mathcal{L}_M = \int_0^M j_m dm$ [$\text{g cm}^2 \text{s}^{-1}$], where $j_m = 2/3 \Omega_m r_m^2$ [$\text{cm}^2 \text{s}^{-1}$] is the specific angular momentum at mass coordinate m . The momentum of inertia of a core of mass M , $\mathcal{I}_M = \int_0^M 2/3 r^2 dm$ [g cm^2].

The properties of the models are presented in four tables: Table 4 for the metallicity of the Small Magellanic Cloud (SMC, $Z = 0.004$), Table 5 for the Large Magellanic Cloud (LMC, $Z = 0.008$), Table 6 for solar metallicity ($Z = 0.020$), and Table 7 for the Galactic centre (GC, $Z = 0.040$). In these tables, for each model we give the initial mass and velocity, as well as the remnant mass estimated from the carbon-oxygen (CO) core mass, using the relation from Maeder (1992). We used the value of the CO core at the end of the evolution for the calculation (at the end of core He-burning in general and at the end of Si-burning for the models from Paper XII). Then,

- Col. 1 is the evolutionary stage to which the values correspond;
- Col. 2 is the total mass at the given stage;
- Col. 3 is the angular momentum contained in the remnant; $\mathcal{L}_{\text{rem}} = \int_0^{M_{\text{rem}}} 2/3 \Omega r^2 dm$ in units of 10^{50} [$\text{g cm}^2 \text{s}^{-1}$];
- Col. 4 is the moment of inertia of the remnant, $\mathcal{I}_{\text{rem}} = \int_0^{M_{\text{rem}}} 2/3 r^2 dm$ in units of 10^{55} [g cm^2];
- Col. 5 is the specific angular momentum at the remnant edge, j_{rem} , in units of 10^{16} [$\text{cm}^2 \text{s}^{-1}$];
- Col. 6 is the average specific angular momentum in the remnant, $\bar{j}_{\text{rem}} = \mathcal{L}_{\text{rem}}/M_{\text{rem}}$, in units of 10^{16} [$\text{cm}^2 \text{s}^{-1}$];
- Col. 7 is the specific angular momentum at the mass coordinate $1.56 M_{\odot}$, $j_{1.56}$, in units of 10^{16} [$\text{cm}^2 \text{s}^{-1}$];
- Col. 8 is the angular momentum contained in the inner $1.56 M_{\odot}$, $\mathcal{L}_{1.56} = \int_0^{1.56 M_{\odot}} 2/3 \Omega r^2 dm$ in units of 10^{50} [$\text{g cm}^2 \text{s}^{-1}$];
- Col. 9 is the specific angular momentum at the mass coordinate $2.5 M_{\odot}$, $j_{2.5}$, in units of 10^{16} [$\text{cm}^2 \text{s}^{-1}$];
- Col. 10 is the angular momentum contained in the inner $2.5 M_{\odot}$, $\mathcal{L}_{2.5} = \int_0^{2.5 M_{\odot}} 2/3 \Omega r^2 dm$ in units of 10^{50} [$\text{g cm}^2 \text{s}^{-1}$].

Assuming that a neutron star with a baryonic mass, $M_b = 1.56 M_\odot$, and with a radius, $R = 12$ km, would form from the models, we calculated the two following quantities:

- (Col. 11) the ratio of the NS angular velocity to its Keplerian angular velocity, $\Omega/\Omega_K(\text{NS})$;
- (Col. 12) the initial rotation period of the neutron star, \mathcal{P}_{rot} in units of milli-seconds.

A proto-neutron star with a baryonic mass, $M_b = 1.56 M_\odot$, loses a binding energy (BE) of $0.159 M_\odot$ due to neutrino emission. This value is calculated using Eq. (36) from Lattimer & Prakash (2001): $\text{BE}/M = 0.6\beta/(1 - 0.5\beta)$, in which $M = M_g$ corresponds to the gravitational mass and where $\beta = GM_g/Rc^2$, and using the fact that $M_b = \text{BE} + M_g$. These equations give one second degree equation:

$$0.1 GM_g^2 - (Rc^2 + 0.5 GM_b)M_g - Rc^2 M_b = 0 \quad (1)$$

from which we can find the gravitational mass, $M_g = 1.401 M_\odot$, which is very close to the average observational value of neutron star (gravitational) masses (Kaper & van der Meer 2005). This is why we chose the value of 1.56 for the baryonic mass. The radius of 12 km was estimated using Fig. 2 from Lattimer & Prakash (2001). The NS momentum of inertia is calculated using Eq. (29) from Lattimer & Prakash (2001), which for the mass and radius chosen here corresponds to $I_{\text{NS}}(\text{TVII})/MR^2 \simeq 0.36$. Since the core loses mass during the collapse, it also loses angular momentum. We assumed here that the angular momentum loss due to neutrino losses is proportional to the quantity of mass lost. Therefore the angular momentum of the NS, $\mathcal{L}_{\text{NS}} = \mathcal{L}_{1.56}(M_g/M_b)$. This assumes that neutrinos are emitted uniformly from the entire core. This is probably correct but additional angular momentum may be lost due to the interaction of these neutrinos with the outer layers of the core (Heger et al. 2005).

Assuming uniform rotation in the neutron star and using the relation $\mathcal{L}_{\text{NS}} = I_{\text{NS}} \Omega_{\text{NS}}$, we have $\Omega_{\text{NS}} = \mathcal{L}_{\text{NS}}/I_{\text{NS}}$. Taking into account no angular momentum losses other than those due to neutrinos described above,

$$\Omega_{\text{NS}} = \mathcal{L}_{1.56}(M_g/M_b)/(0.36 R^2 M_g) = \mathcal{L}_{1.56}/(0.36 R^2 M_b).$$

The Keplerian angular velocity is $\Omega_K = \sqrt{GM_g/R^3}$. Finally, the initial period of rotation of the neutron star is given by $\mathcal{P}_{\text{rot}} = 2\pi/\Omega_{\text{NS}}$.

We also give values of the angular momentum at and in the inner $2.5 M_\odot$, near the maximum mass for NSs. These results allow us to compare different models at a given mass coordinate rather than at the remnant edges, which span a wide range of masses (see Tables 4–7). Finally, we used Eq. (1) to obtain the gravitational masses, M_g and the BE (all in M_\odot units, $M_\odot c^2 = 1.79 \times 10^{54}$ erg) for our models using $R = 15.12 M_b^{-1/3}$ (Newtonian polytropes Shapiro & Teukolsky 1983, p. 245). These values are given in Table 1, and the gravitational masses are shown in Fig. 1. We see that with our estimates BHs are expected to form from stars with masses above about $20 M_\odot$ for solar or lower metallicities. At higher metallicities, the formation of a black hole or neutron star depends on the mass loss prescription. At $Z = 0.040$ and using a mass loss

Table 1. Baryonic masses, M_b , gravitational masses, M_g and the BE (all in M_\odot units, $M_\odot c^2 = 1.79 \times 10^{54}$ erg) of the different models calculated using Eq. (1) and $R = 15.12 M_b^{-1/3}$ (Newtonian polytropes Shapiro & Teukolsky 1983, p. 245).

M_{ini}	M_b	M_g	BE
$Z = 0.004$			
30	3.7284	2.8140	0.9144
40	5.3954	3.5430	1.8524
60	8.5150	4.3964	4.1186
60 ^a	3.7916	2.8464	0.9452
120	5.1429	3.4478	1.6951
$Z = 0.008$			
30	3.7256	2.8125	0.9130
40	5.2110	3.4740	1.7370
60	4.9085	3.3550	1.5535
120	4.0571	2.9780	1.0792
$Z = 0.020$			
9	1.1808	1.1012	0.0796
12	1.4616	1.3338	0.1278
15	1.8496	1.6361	0.2135
20	2.5661	2.1382	0.4280
25	3.0558	2.4424	0.6135
40	3.8527	2.8773	0.9754
60	4.3228	3.1027	1.2201
85	3.7764	2.8386	0.9377
120	3.5392	2.7145	0.8247
$Z = 0.040$			
20	2.6804	2.2119	0.4685
25	3.1257	2.4834	0.6423
40	3.5718	2.7320	0.8399
85	2.5705	2.1410	0.4295
120	2.5329	2.1164	0.4165
$Z = 0.040, \dot{M}_{\text{WR}}(Z)$			
40	3.0225	2.4226	0.5999
60	1.9391	1.7027	0.2364
85	1.9520	1.7122	0.2398
120	1.9637	1.7208	0.2429

^a With $v_{\text{ini}} = 500 \text{ km s}^{-1}$.

dependent on metallicity (models MZ), we expect black hole to form from stars with masses between about 20 and $55 M_\odot$.

3. Evolution of rotation

In Paper XII, we presented the evolution of the angular velocity profiles through the pre-supernova stages for the solar metallicity $25 M_\odot$ model and showed that the angular velocity increases in the core via successive contractions. In the outer part of the star, after the MS, Ω either has very low values when the star is a red supergiant (RSG), or has values similar to the initial values when the H-rich envelope of the star is lost and

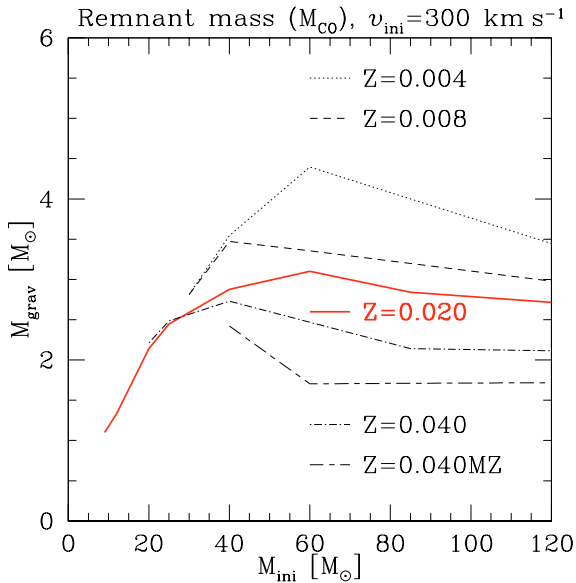


Fig. 1. Remnant gravitational masses (estimated from the CO core masses) as a function of the initial mass of the models.

the star becomes a WR star. If a star is very massive, the star may become a WR before the end of the main sequence (MS) and skip the RSG phase (see Fig. 2). This point has important consequences for the braking of stars by magnetic fields, as mentioned in Heger et al. (2005). Indeed in the theory elaborated by Spruit (2002), differential rotation produces strong magnetic fields, which in turn slow down the core of the star. This means that stars that go through the RSG phase will experience a strong braking due to the large differential rotation between the core and the envelope, while stars that skip the RSG stage might be slowed down much less.

The evolution of the angular momentum profiles has also been discussed in Paper XII. In our models, we consider three transport processes: convection, shear diffusion, and meridional circulation. Convection makes Ω constant and therefore transports angular momentum from the inner part of a convective zone to the outer part of the same convective zone. Shear diffusion reduces differential rotation and also transports angular momentum outwards. Meridional circulation can transport angular momentum inwards or outwards. Mass loss acts somewhat indirectly on the angular momentum of the core by affecting Ω and the gradients of Ω inside the star and thus the efficiency of the transport processes. The main conclusions about the evolution of the angular momentum are the following:

- the angular momentum generally decreases throughout the pre-supernova evolution;
- the largest decrease occurs during the MS;
- after He-burning, only convective zones reshape the angular momentum profile and produce teeth along its profile (redistributing angular momentum from the inner part of a convective zone to the outer part of the same zone) without removing significant amount of angular momentum from the core. This shows that the angular momentum at the end of He-burning is a good approximation of the angular momentum contained in the core at the collapse.

3.1. Dependence on the initial mass

The variation of both the remnant mass and the specific angular momentum as a function of the mass coordinate makes comparison between different models quite difficult at the pre-supernova stage (see Fig. 3). Indeed, the specific angular momentum, j , varies significantly in the core (see Fig. 7 in Paper XII). Until the end of He-burning, j increases monotonically with the mass coordinate. At the end of Si-burning, the teeth produced by the convective zones make the final j at a given mass coordinate oscillate between values slightly above or a few times under the values at the end of He-burning. The remnant mass also obviously varies with the initial mass (see values in Tables 4–7). This is why we also give the values of the specific angular momentum at fixed Lagrangian mass coordinates (1.56 and 2.5) and give the average value inside the remnant (\bar{j}_{rem}). It is easier to compare between models at the end of He-burning, which is what we do in the next section. Nevertheless, we present the values at the end of Si-burning for solar metallicity models to show how the specific angular momentum at a given mass coordinate can vary during the advanced stages.

The general dependence on the initial mass of the final specific angular momentum in the core can be seen in Fig. 3. The larger the initial mass, the smaller the final specific angular momentum in the core, due to a stronger mass loss and a more efficient transport of angular momentum out of the core. The more efficient transport in more massive stars can be explained by the smaller compactness of these stars. Indeed, higher compactness reduces the outward transport by meridional circulation (Gratton-Öpik term proportional to ρ^{-1} , see Paper VII).

3.2. Dependence on the metallicity

Figure 4 shows the initial and final angular momentum profiles (as a function of the Lagrangian mass coordinate) for $40 M_{\odot}$ models at metallicities equal to 0.004 (SMC) and 0.040 (Galactic centre). Since higher metallicity implies stronger mass loss and less compact stars, the dependence of the final specific angular momentum in the core on the metallicity is similar to the dependence on the initial mass of the star. Therefore, the higher the metallicity, the smaller the final angular momentum in the core.

4. Models at the final stages and predictions for long soft gamma-ray bursts (GRBs)

Stellar mass black hole candidates (Cyg X–3, LMC X–1, ...) are mostly observed in X-ray binaries (see Kaper & van der Meer 2005, and references therein). Usually, a lower limit for the mass of the accreting body, which is larger than about 2 to 3 solar masses, makes it a BH candidate. Observationally derived masses range from about 3 to $15 M_{\odot}$ (for GRS1915+105). The gravitational masses in Fig. 1 (and Table 1) can give us a very rough idea of which models may form BHs. BHs are expected to form from stars with masses above about $20 M_{\odot}$. The upper mass limit for BH formation depends on the mass loss prescription. At $Z = 0.040$, and using a mass loss dependent on

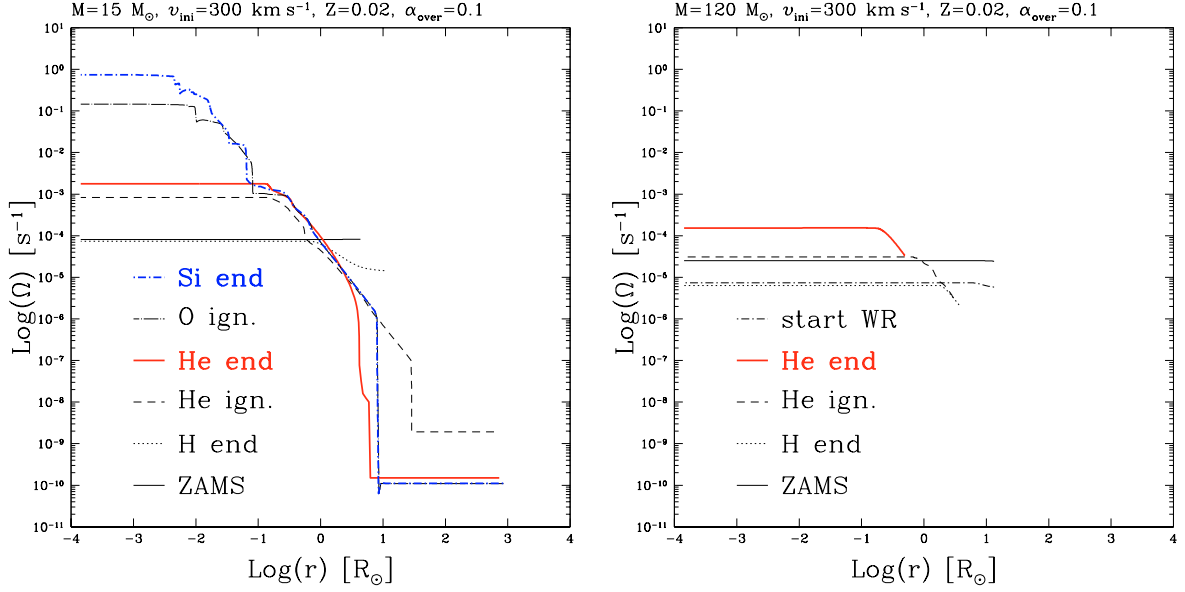


Fig. 2. Evolution of the angular velocity as a function of the radius at different stages of the evolution. *Left:* the $15 M_{\odot}$ model becomes and ends up as a RSG. It therefore has a strong differential rotation between the core and the envelope. *Right:* the $120 M_{\odot}$ model becomes a WR before the end of the MS and will not go through the RSG stage. This last model does not have a strong differential rotation between the core and the envelope and should not be slowed down significantly by magnetic fields.

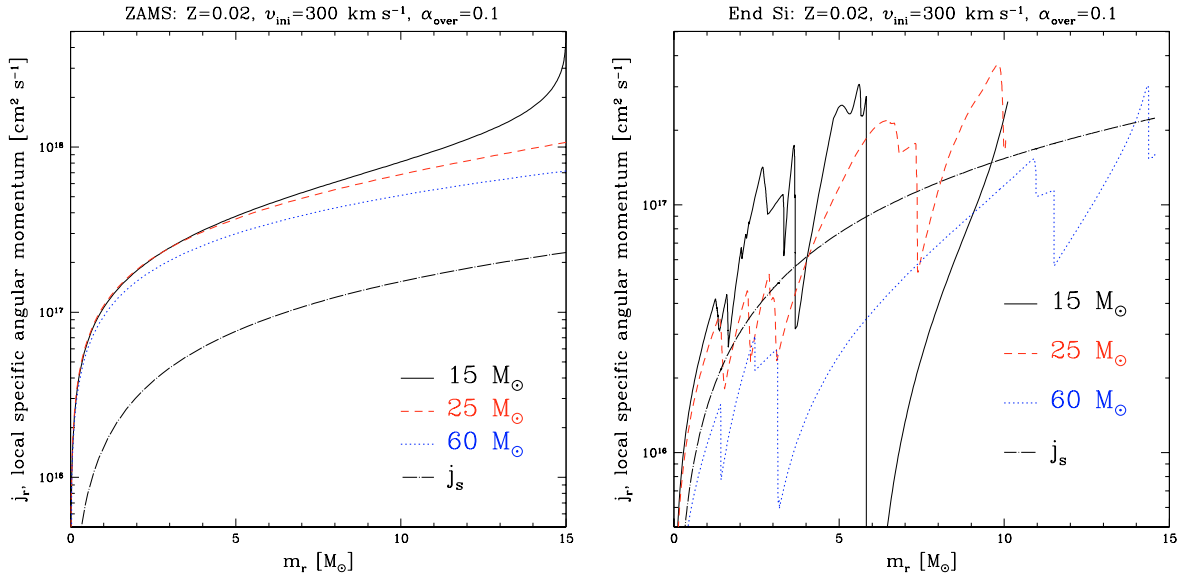


Fig. 3. Profiles of the specific angular momentum, j_r , as a function of the Lagrangian mass coordinate, m , for different models: $15 M_{\odot}$ (solid lines), $25 M_{\odot}$ (dashed lines), and $60 M_{\odot}$ (dotted lines). *Left:* on the ZAMS. *Right:* at the end of Si-burning. $j_s = \sqrt{12} G m / c$ (dashed-dotted line) is the specific angular momentum necessary for matter to form an accretion disk around a non-rotating black hole (Schwarzschild metric) and is displayed here as a reference profile. The specific angular momentum varies significantly with the mass coordinate at the end of Si-burning. For the average profile, the heavier the initial mass of the star, the stronger the mass loss and angular momentum loss. Therefore the core of the $60 M_{\odot}$ model ends with much less angular momentum than on the ZAMS and loses more angular momentum in comparison with lighter models ($15, 25 M_{\odot}$).

metallicity (models MZ), we expect black hole to form from stars with masses between about 20 and $55 M_{\odot}$ (considering models with remnant masses larger than $2 M_{\odot}$ in Fig. 1).

No observation of BH rotation is available. Theoretically, one can use the Kerr metric to describe rotating black holes. In this metric, the parameter $a = Jc/GM$ denotes the angular momentum per unit mass (in units of gram if the other quantities are in CGS units: G , the gravitational

constant, equals $6.67 \times 10^{-8} \text{ cm}^3 \text{ s}^{-2} \text{ g}^{-1}$, c , the speed of light, equals $2.9979 \times 10^{10} \text{ cm s}^{-1}$, M , the remnant mass, is in grams and J , the angular momentum of the remnant is in $\text{g cm}^2 \text{ s}^{-1}$). In the Kerr metric, a/M can take values between 0 (non-rotating BH: the Kerr metric becomes equivalent to the Schwarzschild metric) and 1 (1 for maximally rotating BHs). Figure 5 (right) shows the predicted values for a/M , assuming no loss of angular momentum during collapse (apart from

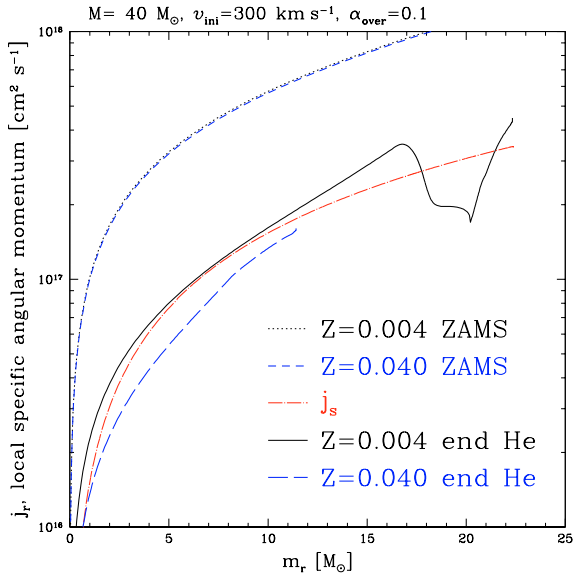


Fig. 4. Profiles of the specific angular momentum, j_r , as a function of the Lagrangian mass coordinate, m , at the ZAMS and at the end of He-burning for $40 M_\odot$ models at $Z = 0.004$ and $Z = 0.040$. The metallicity dependence of the mass loss affects the evolution of the profile, especially at the surface. The decrease of angular momentum is larger at higher metallicity due to a larger mass loss and a more efficient transport. The specific angular momentum necessary to form an accretion disk around a non-rotating black hole (Schwarzschild metric), $j_s = \sqrt{12} GM/c$ is given for reference. We see that a low metallicity star is more likely to form an accretion disk than a high metallicity star.

a uniform loss due to neutrino emission). Stars lighter than about $20 M_\odot$ probably form neutron stars. We see that models between 20 and $60 M_\odot$ have values that exceed the maximal value. These models probably form an accretion disk before the black hole is fully formed.

Accretion disks around BHs are very interesting in the context of long soft GRBs. These bursts were recently connected with SNe of type Ib,c (see Matheson 2003, for example). Three current scenarios (Woosley & Heger 2003) for GRB production are the supranovae model (Vietri & Stella 1999), the magnetar model (Wheeler et al. 2002), and the collapsar mechanism (Woosley 1993). In this last mechanism, a star collapses into a black hole and an accretion disk due to the high angular momentum of the core. Accretion from the disk onto the central black hole produces bi-polar jets. These jets can only reach the surface of the star (and be detected) if the star loses its hydrogen rich envelope before the collapse. WR stars are therefore good candidates for collapsar progenitors, since they lose their hydrogen rich envelope during the pre-SN evolution. Which WR stars form BHs and which have enough angular momentum to form an accretion disk around them? The first part of the question can be answered by looking at the estimated gravitational mass of the remnants presented in Fig. 1 and given in Table 1. In this study, using our rough estimate for the remnant mass, the minimum initial mass for black hole formation is between $20 M_\odot$ ($2 M_\odot$ as the maximum mass for neutron stars) and around $30 M_\odot$ ($2.5 M_\odot$). We use the lower limit of $20 M_\odot$ for GRB rate predictions. For the

following discussion note that the present WO models definitely form BHs. In order to form an accretion disk around a BH, the matter on the last stable orbit (LSO) must have an angular momentum larger than $j_K = r_{\text{LSO}} c$ (Shapiro & Teukolsky 1983, p. 428). The radius of the last stable orbit, r_{LSO} , is given by r_{ms} in formula (12.7.24) from Shapiro & Teukolsky (1983, p. 362) for circular orbit in the Kerr metric. r_{LSO} depends on a and the direction of the orbit. We consider direct (co-rotating) orbits here. In this case r_{LSO} varies from GM/c^2 for $a = 1$ to $5GM/c^2$ for $a = 0$. Note that, for the Schwarzschild metric, $r_{\text{LSO}} = \sqrt{12} GM/c^2$ and $j_s = \sqrt{12} GM/c$. For models with $a > M$, we used $r_{\text{LSO}} = GM/c^2$. Figure 5 (left) shows the specific angular momentum at the edge of the remnant, j_{rem} , for the different models. The values are derived from models at the end of He-burning. For solar metallicity models, values determined at the end of Si-burning are also given. At the edge of the remnant, the specific angular momentum at the end of Si-burning is usually smaller than at the end of He-burning, but it can also be slightly larger as is the case for the $20 M_\odot$ model here. We therefore use values at the end of He-burning for our discussion.

Between 15 and about $40 M_\odot$, j_{rem} increases (see Fig. 5), due to the increase in the remnant size and to the fact that the specific angular momentum increases with mass coordinate (see Fig. 4). If we look at the same mass range in Fig. 6, we see that the lower mass stars rotate faster with respect to break-up rotation than do heavier stars. In fact, the trend is monotonic: the heavier the star, the slower it rotates, compared to a maximally rotating BH. This is true not only at the remnant edge but also at different mass coordinates: $1.56 M_\odot$ (see Tables 4–7) and $2.5 M_\odot$ (see Fig. 6 bottom-left). Even though this trend is already present on the ZAMS (see Fig. 6 top-left), it is much weaker and the evolution is responsible for the final results. As said earlier, the stronger mass loss and more efficient transport of angular momentum are responsible for the lower final angular momentum in the core for high mass models. For the metallicity dependence, Fig. 6 (top-left) shows that lower metallicity models with a same initial mass start with a smaller ratio j/j_K (and end with a higher one). The lower initial ratio is mainly due to the different (higher) remnant mass. Indeed, j_K is proportional to the remnant mass and $j = \Omega r^2$ is roughly proportional to $M_{\text{rem}}^{2/3}$ (if Ω and ρ are constant), which means that the ratio j/j_K is roughly proportional to $M_{\text{rem}}^{-1/3}$. The lower metallicity models that have larger remnant masses start with a smaller ratio. In this study we choose the same initial surface velocity for models of different compactness (lower metallicity = higher compactness) and not the same angular momentum or same ratios j/j_K or Ω/Ω_c . Future studies will consider models with similar angular momentum or ratios, as well as identical velocity, which is very important for extremely low metallicity stars. Even if high metallicity models begin with a higher ratio, they end with a smaller one. Therefore, the trend of higher metallicity leading to smaller final angular momentum (compared to the break-up value) is confirmed.

Concerning the criterion of angular momentum for GRB production, our models show that the lower the initial mass, the more probable the GRB production. The specific angular momentum necessary to form an accretion disk around

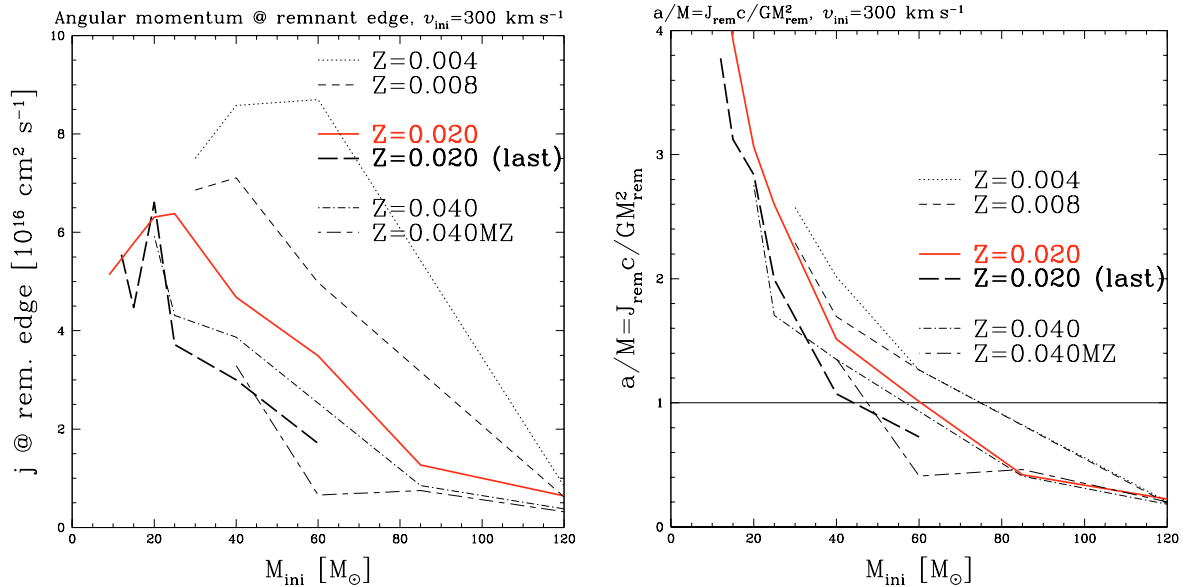


Fig. 5. *Left:* specific angular momentum at the edge of the remnant as a function of the initial mass of the models. The values are determined from the models at the end of He-burning. For solar metallicity models, values determined at the end of Si-burning (last) are also given. Short-long dashed lines represent models with $Z = 0.040$ with a mass loss during the WR phase, which depends on the metallicity (MZ, see Meynet & Maeder 2005). At the edge of the remnant, values at the end of Si-burning are usually lower than at the end of He-burning, but they can also be slightly larger as is the case for the $20 M_{\odot}$ model here. *Right:* angular momentum per unit mass, $a = Jc/GM$, divided by the mass of the remnant, M , as a function of the initial mass of the models. The horizontal line with $a/M = 1$ corresponds to the maximally rotating BHs.

a BH depends on the rotation of the BH itself. If we want to remove this dependence, we can compare j_{rem} with the Schwarzschild metric $j_s = \sqrt{12}GM/c$ (see Fig. 6 bottom-right) although a rotating collapsing core must form a rotating black hole. In this j/j_s plot, the maximally rotating BH value of $j_K/j_s = 1/\sqrt{12}$ is given for reference. This plot shows that models below about $40 M_{\odot}$ even have j/j_s values larger than one.

4.1. Predicted rates of long soft gamma-ray bursts (GRBs) from single star progenitors

Following the method used in Podsiadlowski et al. (2004), we present in Table 2 predictions of the rate of long soft GRBs produced in the collapse of massive single stars. For reference, we use the following SN rate: $\mathcal{R}_{\text{SN}}^{\text{OBS}} = c_{\text{SFR}} \int_{10 M_{\odot}}^{150 M_{\odot}} m^{-2.35} dm = 7 \times 10^{-3} \text{ yr}^{-1}$ ($= c_{\text{SFR}} [150^{-1.35} - 10^{-1.35}] / -1.35$). The value of $7 \times 10^{-3} \text{ yr}^{-1}$ is the same as in Podsiadlowski et al. (2004) and represents the total number of core collapse SNe per year for an average galaxy, while the Milky Way galaxy has a slightly higher value $\sim 1.2 \times 10^{-2} \text{ yr}^{-1}$, see Cappellaro et al. (1999). c_{SFR} is a normalisation factor taking the star formation rate (SFR) into account. It is determined by the equation above. We use Salpeter’s IMF (Salpeter 1955) and an upper mass limit of $150 M_{\odot}$ following the recent results (see Kroupa 2005, and references therein). The other rates are then calibrated to this reference rate: for example, $\mathcal{R}_{\text{GRB}}(\text{WR}) = (7 \times 10^{-3} / \int_{10 M_{\odot}}^{150 M_{\odot}} m^{-2.35} dm) \cdot \int_{M_{\text{GRB}}^{\text{min}}(\text{WR})}^{M_{\text{GRB}}^{\text{max}}(\text{WR})} m^{-2.35} dm$. The rates of WR stars are derived using the minimum mass limits given in Table 2 from Meynet & Maeder (2005).

These minimum masses correspond approximately to the minimum mass for GRB production, since these stars have lost their hydrogen envelope by definition and probably form BHs (have remnant gravitational masses $\gtrsim 2 M_{\odot}$; see Fig. 1 and Table 1). $\mathcal{R}_{\text{GRB}}(\text{WR})$ corresponds to the rate of GRBs produced by massive single stars which form BHs, lose their hydrogen rich envelope, and have enough angular momentum at the edge of the remnant to form an accretion disk. We can see that the rates are much higher (10–1000 times) than the observed long soft GRB rate, $\mathcal{R}_{\text{GRB}}^{\text{OBS}} \approx 3 \times 10^{-6} - 6 \times 10^{-4}$ (Podsiadlowski et al. 2004), for beaming angles between 15 and 1° .

An additional constraint for GRB production might be that the star must be a WR of type WO at the time of the explosion. WO stars are WR stars which have lost not only their hydrogen-rich envelope but also the helium-rich layers. They explode as type Ic supernovae. Although there is no firm evidence to support this fact, the link between GRBs and supernovae was firmly established for the type Ic hypernova SN2003dh (Mazzali et al. 2003). Furthermore, WO stars have lost both their hydrogen and helium-rich layers. This means that their envelope is more tenuous, thus favouring escape of the jets. Smith & Maeder (1991) studied the metallicity dependence of WR stars of type WC and WO to find that the lower the initial metallicity Z , the higher the (C+O)/He number ratio when the star first becomes a WC star. This is due to the fact that at low metallicity, mass loss is smaller and the newly synthesised C and O are revealed later in the evolution. It implies that WO stars are mainly produced at low metallicity. In the present grid of models, no WO star appears at solar or higher metallicities (see Table 3 and Fig. 7). In Fig. 8, we can roughly estimate the mass ranges of WO star formation at the different metallicities. The rate of WO stars and the mass ranges are given in

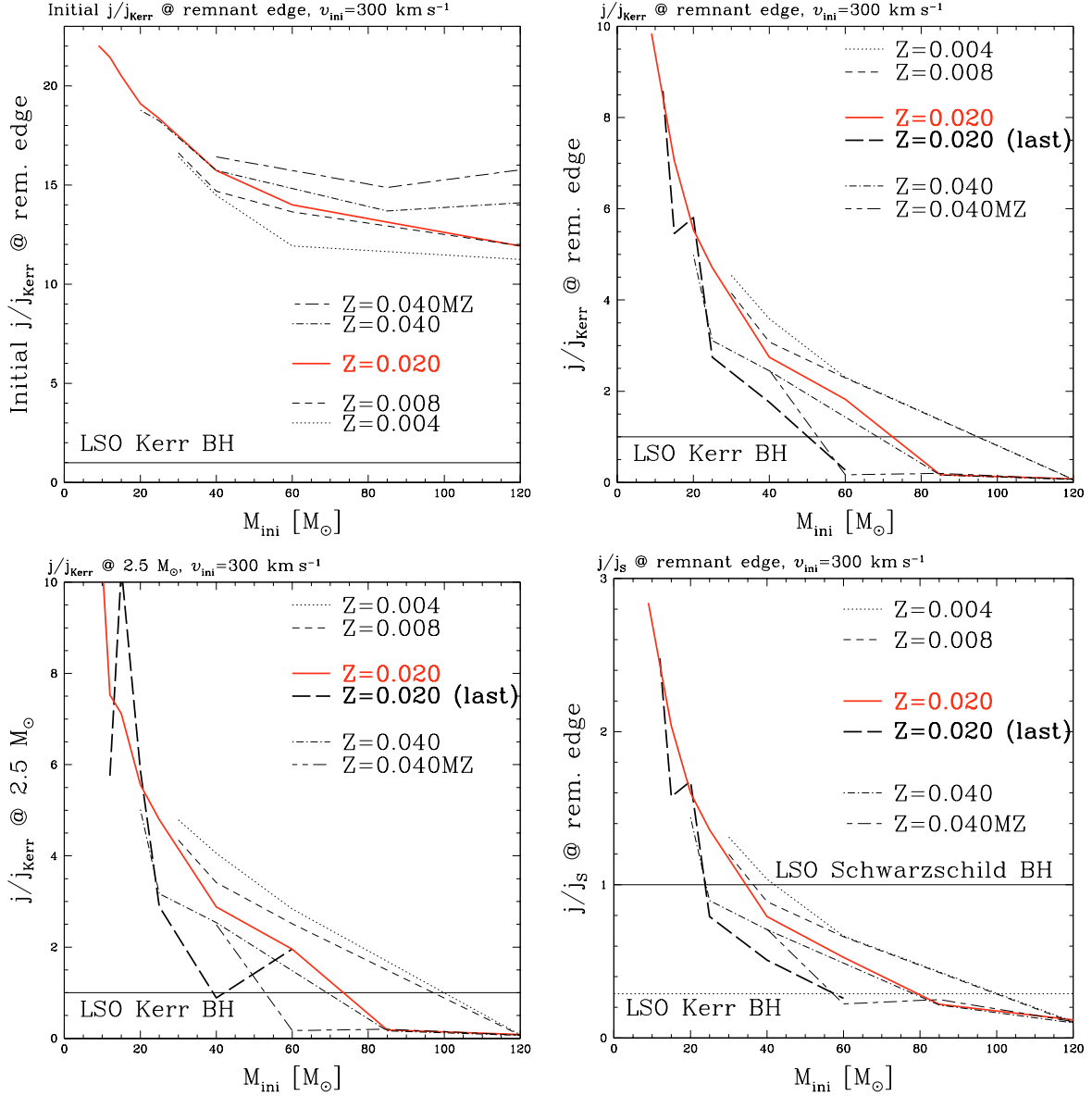


Fig. 6. *Top left:* initial (ZAMS) ratio of the specific angular momentum at the edge of the remnant to $j_{\text{K}} = r_{\text{LSO}} c$ (the value of angular momentum necessary to form an accretion disk at the edge of the remnant) as a function of the initial mass of the models. The initial ratio is shown to see whether trends observed at the end are due to initial conditions or differences in the evolution. *Top right:* final ratio of the specific angular momentum at the edge of the remnant to $j_{\text{K}} = r_{\text{LSO}} c$ as a function of the initial mass of the models. The values are determined from models at the end of He-burning. At solar metallicity, values at the end of Si-burning (last) are also given. *Bottom left:* ratio of the specific angular momentum at the Lagrangian mass coordinate of $2.5 M_{\odot}$ to $j_{\text{K}} = r_{\text{LSO}} c$ as a function of the initial mass of the models. This graph is used to compare models at a fixed Lagrangian mass coordinate. *Bottom right:* ratio of the specific angular momentum at the edge of the remnant to $j_{\text{S}} = \sqrt{12} GM/c$ as a function of the initial mass of the models. In this j/j_{S} plot, the maximally rotating BH value of $j_{\text{K}}/j_{\text{S}} = 1/\sqrt{12}$ is also given for reference. Short-long dashed lines represent models with $Z = 0.040$ with a mass loss during the WR phase, which depends on the metallicity (MZ, see Meynet & Maeder 2005). At the edge of the remnant, values at the end of Si-burning are usually lower than at the end of He-burning, but they can also be slightly larger as is the case for the $20 M_{\odot}$ model here.

Table 2. Combining all the criteria for GRB progenitors, we obtain the predicted rates for GRB production in a normal galaxy coming from WO stars, noted $\mathcal{R}_{\text{GRB}}(\text{WO})$ and given in Table 2.

These rates are upper limits, because we did not convolve our rates with the initial rotational velocity distribution. Indeed slow rotators do not produce GRBs. Very fast rotators may not produce GRBs. As can be seen in Table 4, the final angular momentum contained in the model with $Z = Z_{\text{SMC}}$, an initial mass

of $60 M_{\odot}$ and an initial rotational velocity of 500 km s^{-1} is not sufficient. Magnetic braking may also reduce the mass range for GRB production. However, since the WO stars spend little or no time in the RSG phase and have shorter lifetimes than stars around $15 M_{\odot}$ stars, the magnetic braking may not be as strong for WO as for $15 M_{\odot}$ stars as discussed earlier. Finally, these rates have to be convolved in metallicity to compare with observations. The $\mathcal{R}_{\text{GRB}}(\text{WO})$ rates are in much better

Table 2. Predicted rates [yr^{-1}] of WR stars and of long soft gamma ray bursts (GRBs) from single star progenitors, as well as limiting masses at various metallicities.

	Reference rate: $\mathcal{R}_{\text{SN}}^{\text{OBS}} \simeq 7 \times 10^{-3}$			
	Z_{SMC}	Z_{LMC}	Z_{\odot}	Z_{GC}
\mathcal{R}_{WR}	1.31E-03	1.90E-03	2.29E-03	2.45E-03
\mathcal{R}_{WO}	6.33E-04	7.58E-04	0	0
$M_{\text{GRB}}^{\text{min}}(\text{WR})$	32	25	22	21
$M_{\text{GRB}}^{\text{max}}(\text{WR})$	95	95	75	55
$\mathcal{R}_{\text{GRB}}(\text{WR})$	1.15E-03	1.74E-03	2.01E-03	1.92E-03
$M^{\text{min}}(\text{WO})$	50	45	–	–
$M^{\text{max}}(\text{WO})$	110	100	–	–
\mathcal{R}_{WO}	6.33E-04	7.58E-04	0	0
$M_{\text{GRB}}^{\text{min}}(\text{WO})$	50	45	–	–
$M_{\text{GRB}}^{\text{max}}(\text{WO})$	95	95	–	–
$\mathcal{R}_{\text{GRB}}(\text{WO})$	4.74E-04	5.99E-04	–	–
$\mathcal{R}_{\text{GRB}}^{\text{OBS}} = 3 \times 10^{-6} - 6 \times 10^{-4}{}^a$				

^a Depending on the beaming angle of GRBs.

Table 3. Final WR type for WC/WO stars at various metallicities. At Z_{GC} , models with metallicity dependent mass loss rates were used.

	Z_{SMC}	Z_{LMC}	Z_{\odot}	Z_{GC}
25/30 M_{\odot}	– ^a	WC6	– ^a	WC5
40 M_{\odot}	– ^a	WC4	WC4	WC4
60 M_{\odot}	WO	WO	WC4	WC7
85 M_{\odot}	? ^b	? ^b	WC4	WC6
120 M_{\odot}	WC4	WC4	WC4	WC7

^a “–” means the model does not become a WC or WO star.

^b “?” means the model was not calculated.

agreement anyway with observation than the rates from all WR stars. The very interesting point about WO stars as GRB progenitors is their metallicity dependence. Indeed there is no WO predicted at solar or higher metallicities. At very low metallicities, the existence of WO stars depends on the initial rotational velocity of the stars. If extremely low metallicity stars have the same initial surface velocity as solar metallicity stars, no WO stars can form at extremely low metallicity. However, if the same amount of angular momentum as solar metallicity stars is contained in extremely low metallicity stars, WO stars may form (see Meynet, Ekström and Maeder, in preparation). Observations of host galaxies of GRB show that these galaxies are sub-luminous and blue, pointing in the direction that GRB production is favoured at low metallicity (Le Floch et al. 2003) as is predicted in this study.

5. Conclusion

We present the evolution of rotation in models of massive rotating single stars covering a wide range in mass and metallicity. These models reproduce observations during the early stages of the evolution very well, especially WR populations and

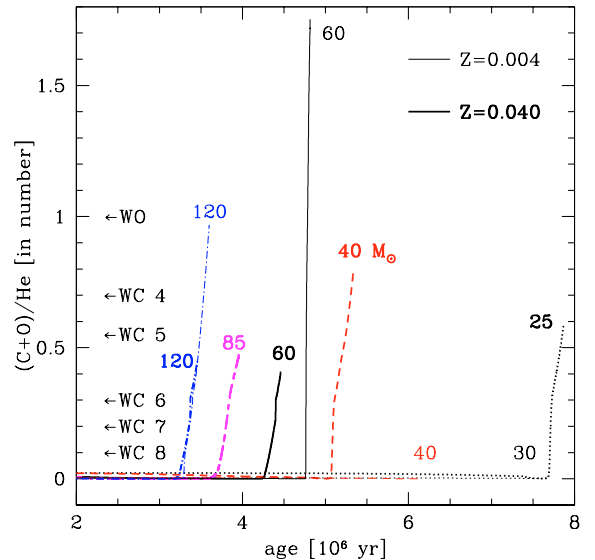


Fig. 7. Evolutionary tracks in the surface (C+O)/He number ratio as a function of age for models with different initial masses at $Z = 0.004$ (thin lines) and $Z = 0.040$ (thick lines). The different WC/WO types are indicated. At $Z = 0.040$, most stars become WC stars but none becomes WO. At $Z = 0.004$, only stars with $M > 60 M_{\odot}$ become WC stars. The $60 M_{\odot}$ becomes a WO star.

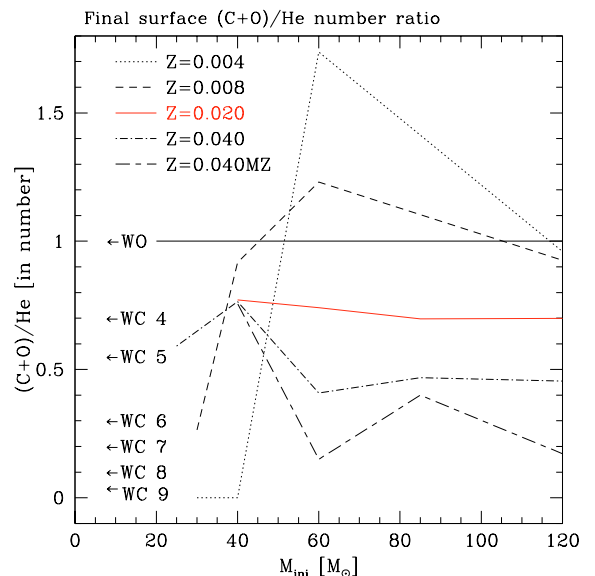


Fig. 8. Final surface (C+O)/He number ratio as a function of the initial mass of the models at different metallicities. WO stars are only found at the metallicities of the Magellanic clouds.

ratio between type II and type Ib,c SNe at different metallicities (see Meynet & Maeder 2005).

Our models predict the production of fast rotating BHs. Models with large initial masses or high metallicity end with less angular momentum in their central remnant with respect to the break-up limit for the remnant. Many WR star models satisfy the three main criteria (BH formation, loss of hydrogen-rich envelope and enough angular momentum to form an accretion disk around the black hole) for long and soft gamma-ray bursts (GRB) production via the collapsar model

(Woosley 1993). Considering all types of WR stars as GRB progenitors, we predict too many GRBs compared to observation. If we consider only WO stars (type Ic supernovae as is the case for SN2003dh/GRB030329, see Mazzali et al. 2003) as GRB progenitors, the GRB production rates are in much better agreement with observations. WO stars are produced only at low metallicities in the present grid of models. Although the numbers estimated in this work are to be taken with caution, the trend in the effects found is clear. The prediction in metallicity dependence can be tested by future observations.

Some recent studies (Heger et al. 2005; Podsiadlowski et al. 2004; Izzard et al. 2004) suggest that single stars cannot retain enough angular momentum for GRB production and predict that binary stars are the progenitors of GRBs. However, Izzard et al. (2004) use a simple description of angular momentum and their models without magnetic braking are not consistent with either our models and those of Heger et al. (2000). Fryer & Heger (2005) study massive binary star mergers in detail. They found that, in general, the final angular momentum contained in the central remnant is similar in merged stars and in single massive stars. Petrovic et al. (2005) find, including the effects of magnetic fields according to Spruit (2002) that, neither the single nor the binary star models that they calculated retain enough angular momentum to form GRBs. Finally, magnetic braking, which is implemented mainly to reproduce the observed pulsar periods (a very important observational constraint), may be much less efficient for WO stars than for NS-forming stars because WO stars spend little or no time in the RSG stage and have shorter lifetimes.

In conclusion, in the present models, the best candidates for GRB progenitors are, for single massive stars, Wolf-Rayet stars of the type WO, which are found only at low metallicities ($Z \sim Z_{\text{SMC}}$) and have masses, $M \gtrsim 50 M_{\odot}$. In order to support this prediction, additional observations are needed to confirm the link between type Ic supernovae and long soft GRBs.

Acknowledgements. R. Hirschi is supported by SNF grant 200020-105328.

References

ATNF. 2005, www.atnf.csiro.au/research/pulsar/psrcat
 Braithwaite, J., & Spruit, H. C. 2004, *Nature*, 431, 819
 Cappellaro, E., Evans, R., & Turatto, M. 1999, *A&A*, 351, 459
 Fryer, C. L. 1999, *ApJ*, 522, 413
 Fryer, C. L., & Heger, A. 2005, *ApJ*, 623, 302
 Fukuda, I. 1982, *PASP*, 94, 271
 Heger, A., Langer, N., & Woosley, S. E. 2000, *ApJ*, 528, 368

Heger, A., Fryer, C. L., Woosley, S. E., Langer, N., & Hartmann, D. H. 2003, *ApJ*, 591, 288
 Heger, A., Woosley, S. E., Langer, N., & Spruit, H. C. 2004, in *Stellar rotation*, IAU Symp., 215, 591 [arXiv:astro-ph/0301374]
 Heger, A., Woosley, S. E., & Spruit, H. C. 2005, *ApJ*, 626, 350
 Hirschi, R., Meynet, G., & Maeder, A. 2004, *A&A*, 425, 649
 Izzard, R. G., Ramirez-Ruiz, E., & Tout, C. A. 2004, *MNRAS*, 348, 1215
 Janka, H.-T., Scheck, L., Kifonidis, K., Müller, E., & Plewa, T. 2005, in *The Fate of the Most Massive Stars*, ASP Conf. Ser., 332, 372 [arXiv:astro-ph/0408439]
 Kaper, L., & van der Meer, A. 2005 [arXiv:astro-ph/0502314]
 Kroupa, P. 2005, *Nature*, 434, 148
 Lattimer, J. M., & Prakash, M. 2001, *ApJ*, 550, 426
 Le Floch, E., Duc, P.-A., Mirabel, I. F., et al. 2003, *A&A*, 400, 499
 MacFadyen, A. I., & Woosley, S. E. 1999, *ApJ*, 524, 262
 Maeder, A. 1992, *A&A*, 264, 105
 Maeder, A., & Meynet, G. 2000, *A&A*, 361, 159
 Maeder, A., & Meynet, G. 2001, *A&A*, 373, 555
 Maeder, A., & Meynet, G. 2004, *A&A*, 422, 225
 Maeder, A., & Meynet, G. 2005, *A&A*, 440, 1041
 Marshall, F. E., Gotthelf, E. V., Zhang, W., Middleditch, J., & Wang, Q. D. 1998, *ApJ*, 499, L179
 Matheson, T. 2003 [arXiv:astro-ph/0309793]
 Mazzali, P. A., Deng, J., Tominaga, N., et al. 2003, *ApJ*, 599, L95
 Meynet, G., & Maeder, A. 1997, *A&A*, 321, 465
 Meynet, G., & Maeder, A. 2002a, *A&A*, 390, 561
 Meynet, G., & Maeder, A. 2002b, *A&A*, 381, L25
 Meynet, G., & Maeder, A. 2003, *A&A*, 404, 975
 Meynet, G., & Maeder, A. 2005, *A&A*, 429, 581
 Morrison, I. A., Baumgarte, T. W., & Shapiro, S. L. 2004, *ApJ*, 610, 941
 Ott, C. D., Ou, S., Tohline, J. E., & Burrows, A. 2005, *ApJ*, 625, L119
 Petrovic, J., Langer, N., Yoon, S.-C., & Heger, A. 2005, *A&A*, 435, 247
 Piran, T. 2005, *Rev. Mod. Phys.*, 76, 1143
 Podsiadlowski, P., Mazzali, P. A., Nomoto, K., Lazzati, D., & Cappellaro, E. 2004, *ApJ*, 607, L17
 Salpeter, E. E. 1955, *ApJ*, 121, 161
 Seward, F. D., Harnden, F. R., & Helfand, D. J. 1984, *ApJ*, 287, L19
 Shapiro, S. L., & Teukolsky, S. A. 1983, *Black-Holes White Dwarfs and Neutron Stars* (John Wiley & Sons)
 Smith, L. F., & Maeder, A. 1991, *A&A*, 241, 77
 Spruit, H. C. 2002, *A&A*, 381, 923
 Srinivasan, G. 2002, *A&AR*, 11, 67
 Staelin, D. H., & Reifstein, E. C. 1968, *Science*, 162, 1481
 Vietri, M., & Stella, L. 1999, *ApJ*, 527, L43
 Wheeler, J. C., Meier, D. L., & Wilson, J. R. 2002, *ApJ*, 568, 807
 Woosley, S. E. 1993, *ApJ*, 405, 273
 Woosley, S. E., & Heger, A. 2003, in *Stellar Rotation*, IAU Symp., 215, 601 [arXiv:astro-ph/0301373]

Online Material

Table 4. $Z = 0.004$ (SMC): angular momenta and momenta of inertia for rotating stellar models at various stages of their evolution. For each model, we give the initial mass and velocity, as well as the remnant mass estimated from the carbon-oxygen (CO) core mass using the relation from Maeder (1992). We used the CO core at the end of the evolution for the calculation: at the end of core He-burning in general and at the end of Si-burning for the models from Paper XII. Column 1 is the evolutionary stage to which the values correspond; Col. 2 is the total mass at the given stage; Col. 3 is the angular momentum contained in the remnant, $\mathcal{L}_{\text{rem}} = \int_0^{M_{\text{rem}}} 2/3 \Omega r^2 dm$ in units of $10^{50} \text{ g cm}^2 \text{ s}^{-1}$; Col. 4 is the moment of inertia of the remnant, $\mathcal{I}_{\text{rem}} = \int_0^{M_{\text{rem}}} r^2 dm$ in units of 10^{55} g cm^2 ; Col. 5 is the specific angular momentum at the remnant edge, j_{rem} , in units of $10^{16} \text{ cm}^2 \text{ s}^{-1}$; Col. 6 is the average specific angular momentum in the remnant, $\bar{j}_{\text{rem}} = \mathcal{L}_{\text{rem}}/M_{\text{rem}}$, in units of $10^{16} \text{ cm}^2 \text{ s}^{-1}$; Col. 7 is the specific angular momentum at the mass coordinate $1.56 M_{\odot}$, $j_{1.56}$, in units of $10^{16} \text{ cm}^2 \text{ s}^{-1}$; Col. 8 is the angular momentum contained in the inner $1.56 M_{\odot}$, $\mathcal{L}_{1.56} = \int_0^{1.56 M_{\odot}} 2/3 \Omega r^2 dm$ in units of $10^{50} \text{ g cm}^2 \text{ s}^{-1}$; Col. 9 is the specific angular momentum at the mass coordinate $2.5 M_{\odot}$, $j_{2.5}$, in units of $10^{16} \text{ cm}^2 \text{ s}^{-1}$; and Col. 10 is the angular momentum contained in the inner $2.5 M_{\odot}$, $\mathcal{L}_{2.5} = \int_0^{2.5 M_{\odot}} 2/3 \Omega r^2 dm$ in units of $10^{50} \text{ g cm}^2 \text{ s}^{-1}$. Assuming that a neutron star with a baryonic mass, $M_b = 1.56 M_{\odot}$, and with a radius, $R = 12 \text{ km}$, would form from the models, we calculated the two following quantities: (Col. 11) the ratio of the NS angular velocity to its Keplerian angular velocity, $\Omega/\Omega_K(\text{NS})$; (Col. 12) the initial rotation period of the neutron star, \mathcal{P}_{rot} in units of milli-seconds.

Stage	Mass	\mathcal{L}_{rem}	\mathcal{I}_{rem}	j_{rem}	\bar{j}_{rem}	$j_{1.56}$	$\mathcal{L}_{1.56}$	$j_{2.5}$	$\mathcal{L}_{2.5}$	$(\Omega/\Omega_{K,\text{NS}})$	$(\mathcal{P}_{\text{rot}})$
	$[M_{\odot}]$	$\frac{\text{g cm}^2}{\text{s}}$	$[\text{g cm}^2]$	$\frac{\text{cm}^2}{\text{s}}$	$\frac{\text{cm}^2}{\text{s}}$	$\frac{\text{cm}^2}{\text{s}}$	$\frac{\text{g cm}^2}{\text{s}}$	$\frac{\text{cm}^2}{\text{s}}$	$\frac{\text{g cm}^2}{\text{s}}$		[ms]
$30 M_{\odot}, v_{\text{ini}} = 300 \text{ km s}^{-1}, M_{\text{rem}} = 3.73 M_{\odot}$											
ZAMS	30.0	11.970	1.8E+00	27.13	16.14	14.24	2.875	20.07	6.190	17.20	0.035
end H	28.7	4.309	4.6E-01	10.06	5.81	5.03	1.003	7.24	2.190	6.00	0.101
start He	28.5	4.123	9.3E-02	9.88	5.56	4.73	0.934	6.94	2.063	5.59	0.108
end He	18.9	3.153	2.8E-02	7.50	4.25	3.64	0.683	5.30	1.534	4.09	0.148
$40 M_{\odot}, v_{\text{ini}} = 300 \text{ km s}^{-1}, M_{\text{rem}} = 5.40 M_{\odot}$											
ZAMS	40.0	21.882	3.8E+00	34.63	20.39	13.86	2.789	19.45	6.164	16.69	0.036
end H	36.8	6.805	1.3E+00	11.05	6.34	4.20	0.839	5.97	1.870	5.02	0.121
start He	36.5	6.367	2.0E-01	10.59	5.93	3.84	0.760	5.52	1.709	4.55	0.133
start WR	27.0	6.012	1.7E-01	9.97	5.60	3.64	0.721	5.22	1.552	4.32	0.140
end He	22.3	5.176	5.4E-02	8.58	4.82	3.13	0.592	4.49	1.337	3.54	0.171
$60 M_{\odot}, v_{\text{ini}} = 300 \text{ km s}^{-1}, M_{\text{rem}} = 8.52 M_{\odot}$											
ZAMS	60.0	44.629	9.7E+00	44.97	26.35	12.95	2.743	18.08	5.775	16.41	0.037
end H	51.8	11.797	3.2E+00	12.16	6.97	3.32	0.700	4.67	1.482	4.19	0.145
start He	50.9	10.968	5.4E-01	11.52	6.48	3.01	0.632	4.26	1.344	3.78	0.160
start WR	44.2	10.697	4.9E-01	11.23	6.32	2.94	0.617	4.16	1.312	3.69	0.164
end He	28.5	8.076	6.2E-02	8.70	4.77	2.21	0.431	3.14	0.945	2.58	0.235
$60 M_{\odot}, v_{\text{ini}} = 500 \text{ km s}^{-1}, M_{\text{rem}} = 3.79 M_{\odot}$											
ZAMS	60.0	18.372	2.5E+00	38.32	24.36	20.33	4.306	28.38	9.066	25.76	0.024
start WR	50.3	4.734	2.1E+00	9.96	6.28	5.21	1.098	7.32	2.322	6.57	0.092
end H	36.7	1.920	8.0E-01	4.23	2.55	2.19	0.461	3.09	0.978	2.76	0.219
start He	36.3	1.754	1.3E-01	3.90	2.33	1.99	0.418	2.83	0.890	2.50	0.242
end He	12.4	1.102	2.8E-02	2.63	1.46	1.24	0.228	1.82	0.518	1.37	0.443
$120 M_{\odot}, v_{\text{ini}} = 300 \text{ km s}^{-1}, M_{\text{rem}} = 5.14 M_{\odot}$											
ZAMS	119.9	16.778	5.4E+00	25.59	16.40	11.09	2.580	15.37	5.408	15.44	0.039
start WR	97.7	5.849	4.6E+00	8.96	5.72	3.85	0.893	5.35	1.876	5.34	0.113
end H	53.0	1.065	1.3E+00	1.73	1.04	0.72	0.154	1.01	0.323	0.92	0.655
start He	52.5	1.052	2.5E-01	1.71	1.03	0.71	0.153	1.00	0.319	0.91	0.664
end He	17.2	0.478	5.3E-02	0.84	0.47	0.31	0.059	0.45	0.131	0.35	1.724

Table 5. $Z = 0.008$ (LMC): angular momenta and momenta of inertia for rotating stellar models at various stages of their evolution (see Table 4 for the legend).

Stage	Mass	\mathcal{L}_{rem}	\mathcal{I}_{rem}	j_{rem}	\bar{j}_{rem}	$j_{1.56}$	$\mathcal{L}_{1.56}$	$j_{2.5}$	$\mathcal{L}_{2.5}$	$(\Omega/\Omega_{\text{K,NS}})$	$(\mathcal{P}_{\text{rot}})$
	$[M_{\odot}]$	10^{50} $\left[\frac{\text{g cm}^2}{\text{s}}\right]$	10^{55} $[\text{g cm}^2]$	10^{16} $\left[\frac{\text{cm}^2}{\text{s}}\right]$	10^{16} $\left[\frac{\text{cm}^2}{\text{s}}\right]$	10^{16} $\left[\frac{\text{cm}^2}{\text{s}}\right]$	10^{50} $\left[\frac{\text{g cm}^2}{\text{s}}\right]$	10^{16} $\left[\frac{\text{cm}^2}{\text{s}}\right]$	10^{50} $\left[\frac{\text{g cm}^2}{\text{s}}\right]$		[ms]
$30 M_{\odot}, v_{\text{ini}} = 300 \text{ km s}^{-1}, M_{\text{rem}} = 3.73 M_{\odot}$											
ZAMS	30.0	12.106	1.9E+00	27.46	16.34	14.42	2.911	20.33	6.268	17.42	0.035
end H	27.5	4.072	5.3E-01	9.51	5.49	4.76	0.949	6.85	2.073	5.68	0.107
start He	27.3	3.880	9.7E-02	9.30	5.24	4.46	0.880	6.54	1.944	5.27	0.115
start WR	16.3	3.365	7.9E-02	8.13	4.54	3.96	0.744	5.77	1.670	4.45	0.136
end He	12.0	2.804	1.1E-02	6.86	3.78	3.27	0.597	4.81	1.381	3.57	0.170
$40 M_{\odot}, v_{\text{ini}} = 300 \text{ km s}^{-1}, M_{\text{rem}} = 5.21 M_{\odot}$											
ZAMS	40.0	20.719	3.9E+00	33.88	19.99	13.93	2.803	19.54	6.193	16.77	0.036
end H	35.3	5.935	1.2E+00	9.95	5.73	3.90	0.777	5.54	1.733	4.65	0.130
start He	34.8	5.510	2.0E-01	9.45	5.32	3.54	0.701	5.08	1.575	4.19	0.144
start WR	28.1	5.338	1.7E-01	9.14	5.15	3.43	0.680	4.93	1.464	4.07	0.149
end He	17.2	4.052	6.5E-03	7.11	3.91	2.62	0.493	3.78	1.118	2.95	0.205
$60 M_{\odot}, v_{\text{ini}} = 300 \text{ km s}^{-1}, M_{\text{rem}} = 4.91 M_{\odot}$											
ZAMS	60.0	17.965	4.1E+00	29.67	18.40	13.02	2.757	18.17	5.804	16.49	0.037
end H	48.4	5.156	7.7E-01	8.64	5.28	3.68	0.775	5.18	1.642	4.64	0.131
start He	46.9	4.594	2.1E-01	8.02	4.71	3.36	0.705	4.75	1.499	4.22	0.143
start WR	43.8	4.523	1.8E-01	7.90	4.63	3.31	0.694	4.68	1.476	4.16	0.146
end He	16.4	2.688	4.1E-02	4.98	2.75	1.92	0.358	2.78	0.804	2.14	0.283
$120 M_{\odot}, v_{\text{ini}} = 300 \text{ km s}^{-1}, M_{\text{rem}} = 4.06 M_{\odot}$											
ZAMS	119.9	11.385	4.0E+00	21.45	14.11	11.00	2.560	15.25	5.366	15.32	0.040
start WR	93.8	3.394	3.5E+00	6.42	4.21	3.27	0.759	4.55	1.595	4.54	0.133
end H	36.6	0.525	7.5E-01	1.07	0.65	0.53	0.106	0.74	0.235	0.63	0.958
start He	36.3	0.519	1.6E-01	1.06	0.64	0.52	0.104	0.73	0.232	0.62	0.970
end He	13.3	0.277	6.3E-03	0.62	0.34	0.28	0.052	0.41	0.116	0.31	1.950

Table 6. $Z = 0.020$ (solar): angular momenta and momenta of inertia for rotating stellar models at various stages of their evolution (see Table 4 for the legend).

Stage	Mass	\mathcal{L}_{rem}	\mathcal{I}_{rem}	j_{rem}	\bar{j}_{rem}	$j_{1.56}$	$\mathcal{L}_{1.56}$	$j_{2.5}$	$\mathcal{L}_{2.5}$	$(\Omega/\Omega_{\text{K,NS}})$	$(\mathcal{P}_{\text{rot}})$
	$[M_{\odot}]$	$\frac{10^{50}}{\left[\frac{\text{g cm}^2}{\text{s}}\right]}$	$\frac{10^{55}}{\left[\text{g cm}^2\right]}$	$\frac{10^{16}}{\left[\frac{\text{cm}^2}{\text{s}}\right]}$	$\frac{10^{16}}{\left[\frac{\text{cm}^2}{\text{s}}\right]}$	$\frac{10^{16}}{\left[\frac{\text{cm}^2}{\text{s}}\right]}$	$\frac{10^{50}}{\left[\frac{\text{g cm}^2}{\text{s}}\right]}$	$\frac{10^{16}}{\left[\frac{\text{cm}^2}{\text{s}}\right]}$	$\frac{10^{50}}{\left[\frac{\text{g cm}^2}{\text{s}}\right]}$		[ms]
$9 M_{\odot}, v_{\text{ini}} = 300 \text{ km s}^{-1}, M_{\text{rem}} = 1.18 M_{\odot}$											
ZAMS	9.0	1.632	1.5E-01	11.51	6.95	14.30	2.592	21.10	5.924	15.51	0.039
end H	8.8	0.744	7.1E-02	5.49	3.17	7.07	1.196	11.90	2.976	7.16	0.085
start He	8.8	0.719	4.5E-03	5.38	3.06	7.47	1.189	0.71	2.806	7.12	0.085
end He	8.4	0.639	2.1E-03	5.14	2.72	5.75	1.057	13.14	2.640	6.32	0.096
$12 M_{\odot}, v_{\text{ini}} = 300 \text{ km s}^{-1}, M_{\text{rem}} = 1.46 M_{\odot}$											
ZAMS	12.0	2.446	2.7E-01	13.86	8.42	14.57	2.730	21.15	6.063	16.33	0.037
end H	11.5	1.025	1.1E-01	6.05	3.53	6.40	1.149	9.92	2.642	6.88	0.088
start He	11.5	1.021	9.4E-03	5.98	3.51	6.33	1.144	10.23	2.635	6.85	0.088
end He	10.3	0.863	3.8E-03	5.46	2.97	5.84	0.975	8.33	2.325	5.83	0.104
start O	10.2	0.688	4.2E-05	5.53	2.37	6.86	0.821	8.63	2.141	4.91	0.123
$15 M_{\odot}, v_{\text{ini}} = 300 \text{ km s}^{-1}, M_{\text{rem}} = 1.85 M_{\odot}$											
ZAMS	15.0	3.682	4.5E-01	16.79	10.01	14.76	2.762	21.21	6.196	16.52	0.037
end H	14.2	1.455	2.0E-01	6.87	3.95	5.95	1.080	9.02	2.506	6.46	0.094
start He	14.2	1.452	1.8E-02	6.87	3.95	6.19	1.073	8.96	2.500	6.42	0.094
end He	10.4	1.182	6.6E-03	5.78	3.21	4.93	0.872	7.88	2.065	5.22	0.116
end Si	10.3	0.941	1.9E-05	4.47	2.56	4.10	0.729	11.40	2.015	4.36	0.139
$20 M_{\odot}, v_{\text{ini}} = 300 \text{ km s}^{-1}, M_{\text{rem}} = 2.57 M_{\odot}$											
ZAMS	20.0	6.590	9.3E-01	21.73	12.91	14.95	2.896	21.30	6.304	17.33	0.035
end H	18.2	2.322	3.5E-01	7.92	4.55	5.25	0.997	7.74	2.217	5.96	0.102
start He	17.5	2.208	3.7E-02	7.81	4.33	4.97	0.924	7.61	2.105	5.53	0.109
end He	8.8	1.781	1.3E-02	6.31	3.49	4.08	0.740	6.15	1.698	4.43	0.137
end Si	8.8	1.652	6.6E-05	6.61	3.24	2.80	0.627	6.50	1.565	3.75	0.161
$25 M_{\odot}, v_{\text{ini}} = 300 \text{ km s}^{-1}, M_{\text{rem}} = 3.06 M_{\odot}$											
ZAMS	25.0	8.990	1.4E+00	24.85	14.79	15.06	2.976	21.33	6.403	17.81	0.034
end H	21.8	2.898	5.1E-01	8.24	4.77	4.80	0.935	6.97	2.045	5.60	0.108
start He	21.6	2.786	6.5E-02	8.19	4.58	4.55	0.873	6.80	1.944	5.22	0.116
start WR	13.5	2.457	5.3E-02	7.26	4.04	4.11	0.759	6.07	1.714	4.54	0.133
end He	10.2	2.143	2.1E-02	6.38	3.53	3.57	0.658	5.31	1.492	3.94	0.154
end Si	10.0	1.644	7.1E-05	3.72	2.71	1.90	0.600	3.20	1.186	3.59	0.169
$40 M_{\odot}, v_{\text{ini}} = 300 \text{ km s}^{-1}, M_{\text{rem}} = 3.85 M_{\odot}$											
ZAMS	40.0	12.549	2.6E+00	26.82	16.38	13.88	2.793	19.48	6.173	16.71	0.036
end H	32.9	3.035	8.9E-01	6.61	3.96	3.32	0.662	4.71	1.476	3.96	0.153
start He	32.3	2.847	1.3E-01	6.30	3.72	3.07	0.609	4.42	1.348	3.65	0.166
start WR	23.9	2.659	1.0E-01	6.02	3.47	2.95	0.586	4.24	1.260	3.51	0.173
end He	12.7	1.976	3.0E-02	4.68	2.58	2.18	0.407	3.19	0.910	2.44	0.249
end Si	12.6	1.399	2.9E-04	3.00	1.83	1.86	0.361	0.98	0.849	2.16	0.281
$60 M_{\odot}, v_{\text{ini}} = 300 \text{ km s}^{-1}, M_{\text{rem}} = 4.32 M_{\odot}$											
ZAMS	60.0	14.451	3.8E+00	26.77	16.81	12.90	2.732	18.01	5.753	16.35	0.037
start WR	44.4	3.644	3.1E+00	7.08	4.24	3.34	0.705	4.70	1.492	4.22	0.144
end H	31.4	2.548	7.2E-01	5.01	2.96	2.32	0.454	3.28	0.991	2.71	0.223
end He	14.6	1.662	2.0E-02	3.49	1.93	1.49	0.276	2.16	0.622	1.65	0.367
end Si	14.6	1.193	5.0E-04	1.71	1.39	1.00	0.250	2.17	0.615	1.50	0.404
$85 M_{\odot}, v_{\text{ini}} = 300 \text{ km s}^{-1}, M_{\text{rem}} = 3.78 M_{\odot}$											
ZAMS	84.9	10.546	3.4E+00	21.97	14.04	11.79	2.638	16.39	5.461	15.78	0.038
start WR	64.5	4.401	3.1E+00	9.22	5.86	4.90	1.094	6.84	2.271	6.54	0.093
end H	23.6	0.727	5.6E-01	1.67	0.97	0.85	0.161	1.21	0.357	0.97	0.627
end He	12.3	0.528	1.4E-02	1.27	0.70	0.60	0.110	0.88	0.253	0.66	0.917
$120 M_{\odot}, v_{\text{ini}} = 300 \text{ km s}^{-1}, M_{\text{rem}} = 3.54 M_{\odot}$											
ZAMS	119.9	8.802	3.5E+00	18.68	12.50	10.55	2.455	14.63	5.146	14.69	0.041
start WR	87.2	2.344	3.2E+00	4.99	3.33	2.80	0.650	3.90	1.367	3.89	0.156
end H	26.2	0.386	6.1E-01	0.93	0.55	0.50	0.099	0.71	0.214	0.59	1.026
start He	26.0	0.376	1.2E-01	0.91	0.53	0.49	0.096	0.69	0.208	0.57	1.055
end He	11.3	0.248	1.6E-02	0.64	0.35	0.32	0.059	0.47	0.133	0.35	1.719

Table 7. $Z = 0.040$ (GC): angular momenta and momenta of inertia for rotating stellar models at various stages of their evolution (see Table 4 for the legend).

stage	Mass	\mathcal{L}_{rem}	\mathcal{I}_{rem}	j_{rem}	\bar{j}_{rem}	$j_{1.56}$	$\mathcal{L}_{1.56}$	$j_{2.5}$	$\mathcal{L}_{2.5}$	$(\Omega/\Omega_{\text{K,NS}})$	$(\mathcal{P}_{\text{rot}})$
	$[M_{\odot}]$	$\frac{10^{50}}{\left[\frac{\text{g cm}^2}{\text{s}}\right]}$	$\frac{10^{55}}{\left[\text{g cm}^2\right]}$	$\frac{10^{16}}{\left[\frac{\text{cm}^2}{\text{s}}\right]}$	$\frac{10^{16}}{\left[\frac{\text{cm}^2}{\text{s}}\right]}$	$\frac{10^{16}}{\left[\frac{\text{cm}^2}{\text{s}}\right]}$	$\frac{10^{50}}{\left[\frac{\text{g cm}^2}{\text{s}}\right]}$	$\frac{10^{16}}{\left[\frac{\text{cm}^2}{\text{s}}\right]}$	$\frac{10^{50}}{\left[\frac{\text{g cm}^2}{\text{s}}\right]}$		[ms]
$20 M_{\odot}, v_{\text{ini}} = 300 \text{ km s}^{-1}, M_{\text{rem}} = 2.68 M_{\odot}$											
ZAMS	20.0	7.033	1.1E+00	22.27	13.19	14.82	2.869	21.11	6.245	17.17	0.035
end H	16.9	2.223	3.0E-01	7.29	4.17	4.66	0.882	6.87	1.966	5.28	0.115
start He	16.8	2.176	4.8E-02	7.43	4.08	4.52	0.840	6.93	1.915	5.03	0.120
end He	9.2	1.742	1.1E-02	5.92	3.27	3.69	0.670	5.55	1.535	4.01	0.151
$25 M_{\odot}, v_{\text{ini}} = 300 \text{ km s}^{-1}, M_{\text{rem}} = 3.13 M_{\odot}$											
ZAMS	25.0	9.300	1.6E+00	25.26	14.96	15.04	2.977	21.31	6.396	17.81	0.034
end H	21.3	1.980	3.2E-01	5.48	3.18	3.18	0.623	4.58	1.352	3.73	0.163
start He	20.9	1.872	8.4E-02	5.24	3.01	2.99	0.583	4.35	1.273	3.49	0.174
start WR	18.5	1.854	6.6E-02	5.18	2.98	2.96	0.554	4.30	1.249	3.31	0.183
end He	9.6	1.471	1.9E-02	4.31	2.37	2.35	0.424	3.51	0.976	2.54	0.239
$40 M_{\odot}, v_{\text{ini}} = 300 \text{ km s}^{-1}, M_{\text{rem}} = 3.57 M_{\odot}$											
ZAMS	40.0	10.867	2.5E+00	24.86	15.30	13.61	2.737	19.10	6.051	16.38	0.037
start WR	31.1	2.400	1.7E+00	5.74	3.38	3.07	0.612	4.35	1.308	3.66	0.165
end H	29.9	2.343	5.5E-01	5.62	3.30	2.99	0.596	4.25	1.275	3.57	0.170
start He	29.7	2.170	1.2E-01	5.27	3.05	2.75	0.545	3.95	1.172	3.26	0.186
end He	11.4	1.516	2.3E-02	3.87	2.13	1.91	0.356	2.81	0.798	2.13	0.285
$40 M_{\odot}, v_{\text{ini}} = 300 \text{ km s}^{-1}, M_{\text{rem}} = 3.02 M_{\odot}, \dot{M}_{\text{WR}}(Z)$											
ZAMS	40.0	8.250	1.9E+00	21.95	13.72	13.61	2.737	19.10	6.051	16.38	0.037
start WR	31.1	1.804	1.3E+00	5.03	3.00	3.07	0.612	4.35	1.308	3.66	0.165
end H	29.5	1.754	4.0E-01	4.91	2.92	2.98	0.594	4.24	1.271	3.55	0.170
start He	29.2	1.623	8.9E-02	4.59	2.70	2.75	0.544	3.94	1.172	3.26	0.186
end He	9.0	1.087	1.7E-02	3.29	1.81	1.84	0.331	2.76	0.770	1.98	0.305
$60 M_{\odot}, v_{\text{ini}} = 300 \text{ km s}^{-1}, M_{\text{rem}} = 1.94 M_{\odot}, \dot{M}_{\text{WR}}(Z)$											
start WR	44.9	0.971	9.9E-01	3.83	2.52	3.27	0.691	4.60	1.461	4.13	0.146
end H	9.3	0.169	1.3E-01	0.76	0.44	0.63	0.116	0.94	0.265	0.69	0.872
start He	9.1	0.166	3.0E-02	0.75	0.43	0.62	0.114	0.93	0.261	0.68	0.889
end He	4.8	0.136	5.5E-03	0.66	0.35	0.53	0.091	0.87	0.221	0.54	1.111
$85 M_{\odot}, v_{\text{ini}} = 300 \text{ km s}^{-1}, M_{\text{rem}} = 2.57 M_{\odot}$											
ZAMS	84.8	5.316	1.9E+00	15.57	10.40	10.98	2.456	15.27	5.086	14.70	0.041
start WR	62.6	2.056	1.8E+00	6.05	4.02	4.24	0.947	5.93	1.967	5.67	0.107
end H	15.6	0.334	2.5E-01	1.12	0.65	0.75	0.142	1.09	0.318	0.85	0.711
start He	15.3	0.329	5.7E-02	1.11	0.64	0.74	0.140	1.09	0.314	0.84	0.725
end He	7.3	0.237	1.2E-02	0.85	0.46	0.54	0.096	0.83	0.225	0.58	1.051
$85 M_{\odot}, v_{\text{ini}} = 300 \text{ km s}^{-1}, M_{\text{rem}} = 1.95 M_{\odot}, \dot{M}_{\text{WR}}(Z)$											
ZAMS	84.8	3.455	1.3E+00	12.84	8.90	10.98	2.456	15.27	5.086	14.70	0.041
start WR	62.6	1.334	1.2E+00	4.97	3.44	4.24	0.947	5.93	1.967	5.67	0.107
end H	11.6	0.202	1.5E-01	0.90	0.52	0.75	0.137	1.11	0.313	0.82	0.737
start He	11.3	0.204	3.0E-02	0.92	0.53	0.76	0.138	1.14	0.317	0.82	0.735
end He	4.7	0.155	7.2E-03	0.75	0.40	0.60	0.102	0.98	0.249	0.61	0.993
$120 M_{\odot}, v_{\text{ini}} = 300 \text{ km s}^{-1}, M_{\text{rem}} = 2.53 M_{\odot}$											
ZAMS	118.8	5.616	2.2E+00	15.80	11.15	11.29	2.626	15.65	5.505	15.71	0.039
start WR	86.5	1.314	2.1E+00	3.71	2.61	2.64	0.613	3.67	1.287	3.66	0.165
end H	14.0	0.132	3.1E-01	0.45	0.26	0.31	0.058	0.45	0.129	0.35	1.755
start He	13.8	0.130	5.7E-02	0.45	0.26	0.30	0.057	0.44	0.127	0.34	1.784
end He	7.1	0.103	1.3E-02	0.38	0.21	0.24	0.043	0.37	0.101	0.26	2.341
$120 M_{\odot}, v_{\text{ini}} = 300 \text{ km s}^{-1}, M_{\text{rem}} = 1.96 M_{\odot}, \dot{M}_{\text{WR}}(Z)$											
ZAMS	119.6	3.969	1.5E+00	13.68	10.16	11.68	2.717	16.20	5.697	16.26	0.037
start WR	86.5	0.896	1.4E+00	3.10	2.29	2.64	0.613	3.67	1.288	3.67	0.165
end H	9.6	0.083	1.6E-01	0.37	0.21	0.30	0.055	0.45	0.127	0.33	1.842
start He	9.4	0.082	3.1E-02	0.36	0.21	0.30	0.054	0.45	0.126	0.32	1.875
end He	4.8	0.068	6.8E-03	0.32	0.17	0.26	0.044	0.42	0.108	0.26	2.296